
Article:
Chang, X., Smith, G.C., Quinn, J. et al. (3 more authors) (2020) Optimization of anti-wear and anti-bacterial properties of beta TiNb alloy via controlling duty cycle in open-air laser nitriding. Journal of the Mechanical Behavior of Biomedical Materials, 110. 103913. ISSN 1751-6161

https://doi.org/10.1016/j.jmbbm.2020.103913

Optimization of anti-wear and anti-bacterial properties of beta TiNb alloy via controlling duty cycle in open-air laser nitriding

Xianwen Chang[a], Graham C. Smith[b], James Quinn[c], Louise Carson[c],

Chi-Wai Chan [b]*, Seunghwan Lee*[a]

[a]Department of Mechanical Engineering, Technical University of Denmark, DK-2800 Kgs. Lyngby, Denmark

[b]Faculty of Science and Engineering, University of Chester, Thornton Science Park, Chester CH2 4NU, UK

[c]School of Pharmacy, Queen's University Belfast, Belfast BT9 7BL, UK

[d]School of Mechanical and Aerospace Engineering, Queen's University Belfast BT9 5AH, UK

Keywords: beta Ti-Nb alloys, fibre laser nitriding, wear, antibacterial, duty cycle

Correspondences: Dr. Seunghwan Lee (seele@mek.dtu.dk); Dr. Chi-Wai Chan (c.w.chan@qub.ac.uk)

Abstract

A multifunctional beta TiNb surface, featuring wear-resistant and antibacterial properties, was successfully created by means of open-air fibre laser nitriding. Beta TiNb alloy was selected in this study as it has low Young's modulus, is highly biocompatible, and thus can be a promising prosthetic joint material. It is, however, necessary to overcome intrinsically weak mechanical properties and poor wear resistance of beta TiNb in order to cover the range of applications to load-bearing and/or shearing parts. To this end, open-air laser nitriding technique was employed. A control of single processing parameter, namely duty cycle (between 5% and 100%), led to substantially different structural and functional properties of the processed beta TiNb surfaces as analyzed by an array of analytical tools. The TiNb samples nitrided at the DC condition of 60% showed a most enhanced performance in terms of improving surface hardness, anti-friction, anti-wear and anti-bacterial properties in comparison with other conditions. These findings are expected to be highly important and useful when TiNb alloys are considered as materials for hip/knee articular joint implants.

1. Introduction

According to a recent report (Market Report, 2019), the global hip replacement devices market is valued 6,830 million USD in 2018 and will reach 9,490 million USD by the end of 2025. The number of total hip arthroplasty (THA) or total knee arthroplasty (TKA) surgeries is also increasing as shown, for example, in EU (OECD Health Statistics, 2016). A concomitantly growing concern is that the number of younger patients (referring to those ≤ 60 years old) has also been increasing (Steven, 2004) whereas the survival rate of the implants in those age group is particularly low (Per et al.,2016). In turn, this leads to increasing demand of revision surgery (Labek et al., 2011), which is an additional risk and burden to the patients and society. The failure of artificial joint implant is mainly ascribed to two reasons. The first is bacterial infection, in particular by *Staphylococcus aureus* and *Escherichia coli* (Song et al., 2013). Medical device associated infection is increasingly becoming a challenge faced by orthopaedic implants, complicated by the prevalence of antimicrobial resistance. The second is wear debris generated from various tribological contacts between the components of artificial joint implants even in aseptic condition. Examples include relative compressed sliding contacts in bearings of THA or TKA, micro-motions occurring at the junction between the femoral head and stem in THA, and even from "cement" or glue to fix the implants to the bone tissues (Karl, 2011). Accumulation of the wear debris leads to a cascade of unfavorable immunological responses and loosening of the implants (Man et al., 2017). While the influence by bacterial infection is manifested in a relatively short while after surgery, e.g. on the order of a few years, the effect by wear particles takes much longer time, but acts as the major factor to limit the service lifetime of the implants. In order to cope with increasing demand of prolonging the service lifetime of orthopaedic implants as mentioned above, a significant improvement in materials and/or designs is necessary. Given that bacterial infection and wear debris are two major sources of implant failures, it is reasonable to tackle these two problems as a first attempt.

In this context, a material receiving emerging attention is TiNb, a beta Ti-alloy. Compared to Ti6Al4V, the currently dominating material for the parts interfacing with bone tissues, TiNb

alloys have low Young's modulus, which is closer to that of bone tissues. Due to the absence of elements which may pose cytocompatibility issues, such as Al or V present in Ti6Al4V alloy, TiNb offers improved biocompatibility (Samuel et al., 2008). However, it has the conspicuous drawback of low hardness and poor wear resistance. Therefore, its surface needs to be hardened before considering an application as load-bearing and shearing part of articular joint implants. To date, various efforts to harden the surface of Ti alloys have been conducted, and among them, laser nitriding has shown several advantages compared to other techniques, such as no need of specific gas/vacuum systems, high speed, small heat input, and clean processing. This approach has been very effective to create surface hardening of various types of Ti-based alloys (Katayama et al., 1983). Recently, the authors have shown that this approach can be applicable to TiNb surfaces too (Chan et al., 2020). The gold-coloured TiN layers formed by the open-air laser nitriding method in modulation of duty cycle generated a range of TiN layer with varying thickness (22-43μm) and hardness (reaching to 870HV). Moreover, optimization of duty cycle, namely 40% compared to continuous wave (CW) mode, led to the formulation of a crack-free and homogenous nitride surface on TiNb surface. A thorough description on the micro-structure generated on TiNb alloy is presented in the recent study (Chan et al., 2017, Chan et al. 2018, Donaghy et al 2020).

In this study, we have reproduced the formation of laser-nitride layer on beta TiNb surface by open-air laser-nitriding as in the previous study (Chan et al., 2020), but with an extended range of the duty cycles from 5% (modulated mode) to 100% (continuous wave, CW mode). More importantly, the present study focuses on the characterization of functional properties, in particular anti-wear and anti-bacterial properties of laser-nitrided TiNb surfaces. The surface roughness and topography, phase structure, hardness, friction and wear properties, as well as the antibacterial properties of the laser-nitrided surfaces were carefully investigated and systematically compared with each other. In turn, the optimized anti-wear and antibacterial properties of laser-nitrided TiNb surfaces acquired by modulating the duty cycle were discussed in correlation with the optimized structural properties of nitride layers. The findings of this study are expected to be highly important and useful in pursuing the best laser processing conditions to impart required multifunctional

properties to TiNb alloys when they are employed as materials for hip/knee joints implants.

2. Materials and Methods

2.1. Materials prepared for laser nitriding

The material used in the experiments was Ti-45%Nb alloy in the plate form (American Elements, US). The dimensions of the TiNb plate were 50 mm × 125 mm with a thickness of 2 mm. Before laser nitriding, the surfaces were ground and polished by 120, 240, 400, 800, 1000 grit silicon carbide (SiC) papers in a sequential order, followed by ultrasonic cleaning in acetone for 10 min and dried in cool air-flow. Laser nitriding was performed on the original plate, and the laser-nitrided samples were cut out from the plate into smaller size with the dimensions of 10.5 mm × 10.5 mm using a wire-cut electrical discharge machine (EDM).

2.2. Laser nitriding process in open air

The fully automated fiber laser system (MLS-4030, Micro Laser Systems, Netherlands) was utilized for laser nitriding in open air. The laser processing parameters were laser power of 45 W, wavelength of 1.064 μm, scanning speed of 25 mm/s, stand-off distance of 1.5 mm. The laser beam shape is circular, and the laser beam profile is Gaussian. The spot diameter at the stand-off distance we used in the laser experiment (1.5 mm away from the laser nozzle) is 100 μm. The laser fluence at the power of 45 W with the modulation frequency of 100 kHz was estimated to be 5.7 J/cm^2; a detailed calculation on the laser fluence is provided in the Supplementary Material (S1). The modulation frequency of the laser system is 100 kHz, and hence the pulse duration is 10^{-5} s or 10 μs. High purity N_2 was set at the constant pressure of 6 bars. Duty cycle was varied from 5% to 100% with the above parameters kept unchanged. The laser-nitrided samples were denoted as DC5, DC20, DC40, DC60, DC80 and DC100. The samples between DC5 and DC80 were considered as nitrided at the modulated (pulsed) mode while DC100 was nitrided at CW mode. The laser nitriding process was repeated at least three times (n = 3) for each duty cycle condition. The samples treated under lower duty cycle (5% to 20%) appeared in shiny silver colour while gold

colour in a different shade was observed from the samples treated with higher duty cycles between 40% to 100% (Figure 1).

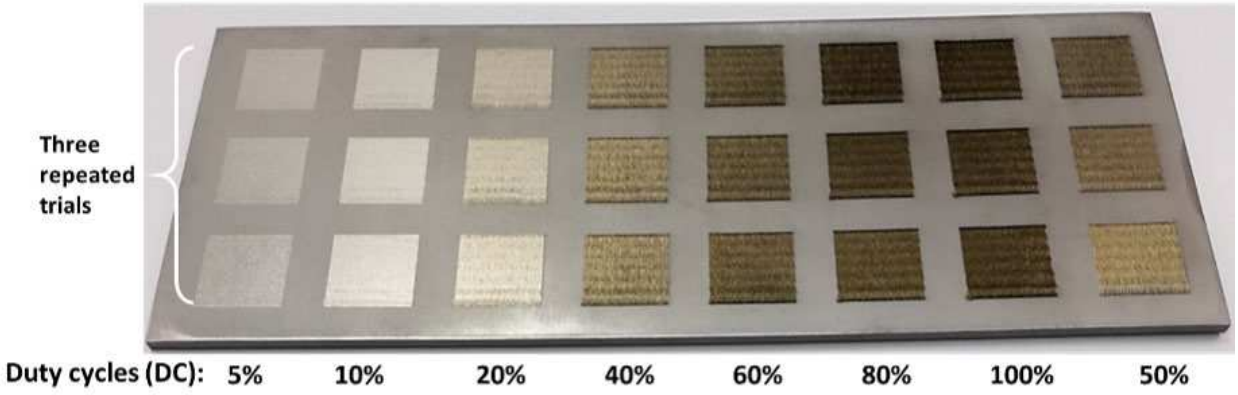

Figure 1. Laser-nitrided TiNb alloy plate treated under different duty cycles (from 5% to 100%, n = 3).

2.3. Phase structure by XRD

Phase identification of the untreated base metal (BM) and laser-nitrided samples was carried out by X-ray diffraction (PANalytical, UK). CuKα radiation source was used with coupled θ - 2θ (Bragg-Brentano) geometry. The diffraction angle 2θ ranged between 20-100°. After the collection of data, diffraction patterns of different samples were compared to the reference material data in the database of the XRD system (International Centre for Diffraction Data) for curve fitting.

2.4. Surface roughness measurement (WLI)

The surface roughness was characterized using white light interferometry (Talysurf CCI 6000, Leicester, Leicestershire, UK). The 3D and 2D profiles in micro scale were generated by TALYMAP software. Two main roughness parameters were Sa (arithmetic mean surface roughness) and Sz (maximum surface roughness) and were extracted from the area of 1.2 mm × 1.2 mm in each sample. The setting of height between the lens and sample surface was set at 100 microns with piezoelectric a-axis control.

2.5. Vickers micro-hardness measurements

Vickers micro-hardness of cross-section of the samples was measured by Vickers hardness tester (Future-Tech Corp, FM-700, Japan). A full load of 10 kgf was applied for 10 seconds in each indentation. The load and distance used in the test were carefully determined according to the location of different zones (laser-nitrided zone, heat affected zone (HAZ) and BM) in the cross-sectioned surface. During the hardness tests, enough space was provided between each indentation mark because the deformation caused by the indents can affect the accuracy of results. Multiple measurement (n = 3) was performed to obtain the average hardness value and standard deviation.

2.6. Tribological properties: Pin-on-disk tribometry and dynamic light scattering (DLS)

Pin-on-disk tribometry (Anton Paar, Tribometer Module 4.4.M) was performed by employing sapphire ball (3 mm in diameter) as slider against Ti disc samples. The Ti disc samples were firstly ultrasonically cleaned, dried in N_2 blow, glued to UHMWPE disc, and dried in air overnight. Fetal Bovine Serum (FBS) was used as simulated synovial fluid in tribological tests. The disc was rotated at the linear speed of 50 mm/s and at the radius of 3 mm from the disc center. A constant load of 10 N was applied to the sample surface and total sliding distance was set at 1000 m. Based on the mechanical properties of tribopair materials, contact geometry, and applied load, apparent maximum Hertzian contact pressures are estimated to range from 2.78 GPa (sapphire ball/TiN pair) to 1.71 GPa (sapphire ball/TiNb (BM) pair) (Supplementary Material, S2). The purpose of this test was two-folded; firstly, the coefficient of friction (COF or μ), defined as friction force/load, was recorded during the entire sliding contact duration. The data acquisition rate was 0.5 Hz. Secondly, after the tribometry tests, the FBS fluids containing wear particles were collected to characterize the size distribution, such as Z-average and hydrodynamic diameter (D) in FBS. The dynamic light scattering (DLS, Malvern Zetasizer Nano) and the corresponding Zetasizer software were utilized in this experiment. For each sample, the measurement was repeated ten times to constitute one trial, and five trial runs were performed for each measurement. The operation temperature was set at 25 °C.

2.7. Surface morphology by optical microscopy (OM)

An optical microscope (ZEISS AXIO Vert A1) was used to capture the images for the hardness tests and for the observation of wear tracks after sliding tests.

2.8. Bacterial cell culture and viability analysis

Bacteria culture

S. aureus (ATCC 35984) was cultured on the base metal (BM) and laser-nitrided samples to study the bacterial adherence and biofilm formation on the surfaces. The samples were firstly cleaned in ultrasonic bath with ethanol (Sigma Aldrich UK) for 15 min and air-dried. Overnight cultures in Müller Hinton broth (MHB) were adjusted to an optical density of 0.3 at 550 nm, then diluted 1 in 50 with fresh MHB. This provides an inoculum of approximately $1x10^6$ cfu/ml. The samples were immersed in this inoculums for 24h at 37°C, with 100rpm shaking in a gyratory incubator.

Bacterial coverage analysis

After 24 hours incubation in bacterial culture, the samples were rinsed three times in sterile PBS to remove any loosely adherent planktonic bacteria. Samples were ten stained by immersing in Live/Dead BacLight^{TM} solution (Molecular Probes) for 30 min. The STYO 9 component of the live/dead staining protocol is a green fluorescent dye that will stain live (viable) bacteria, while propodium iodide (a red fluorescent dye) will only stain nonviable bacteria with damaged membranes. A fluorescence microscope (GXM-L3201 LED; GX Optical) was used to observe the bacterial coverage. Three random fields of view (FOV) for each of the three replicate materials test, with a total of 9 images captured for each treatment condition. Image analysis software (ImageJ, NIH) was used to quantify the areas stained green and red in the images. The total coverage of biofilm was calculated by combining the areas of viable bacteria (green) and non-viable bacteria (red). Statistical analysis was carried out by means of a one-way ANOVA with

Tukey's multiple comparisons post hoc test ($\alpha = 0.05$), using GrapPad Prism (version 8.3.1.)

3. Results and Discussion

3.1. Structural and compositional features

Phase structure before and after laser nitriding

The phase structure of BM and laser-nitrided samples on their top surfaces was identified using XRD in the diffraction angles ranging from 20° to 100°. The results are shown in Figure 2.

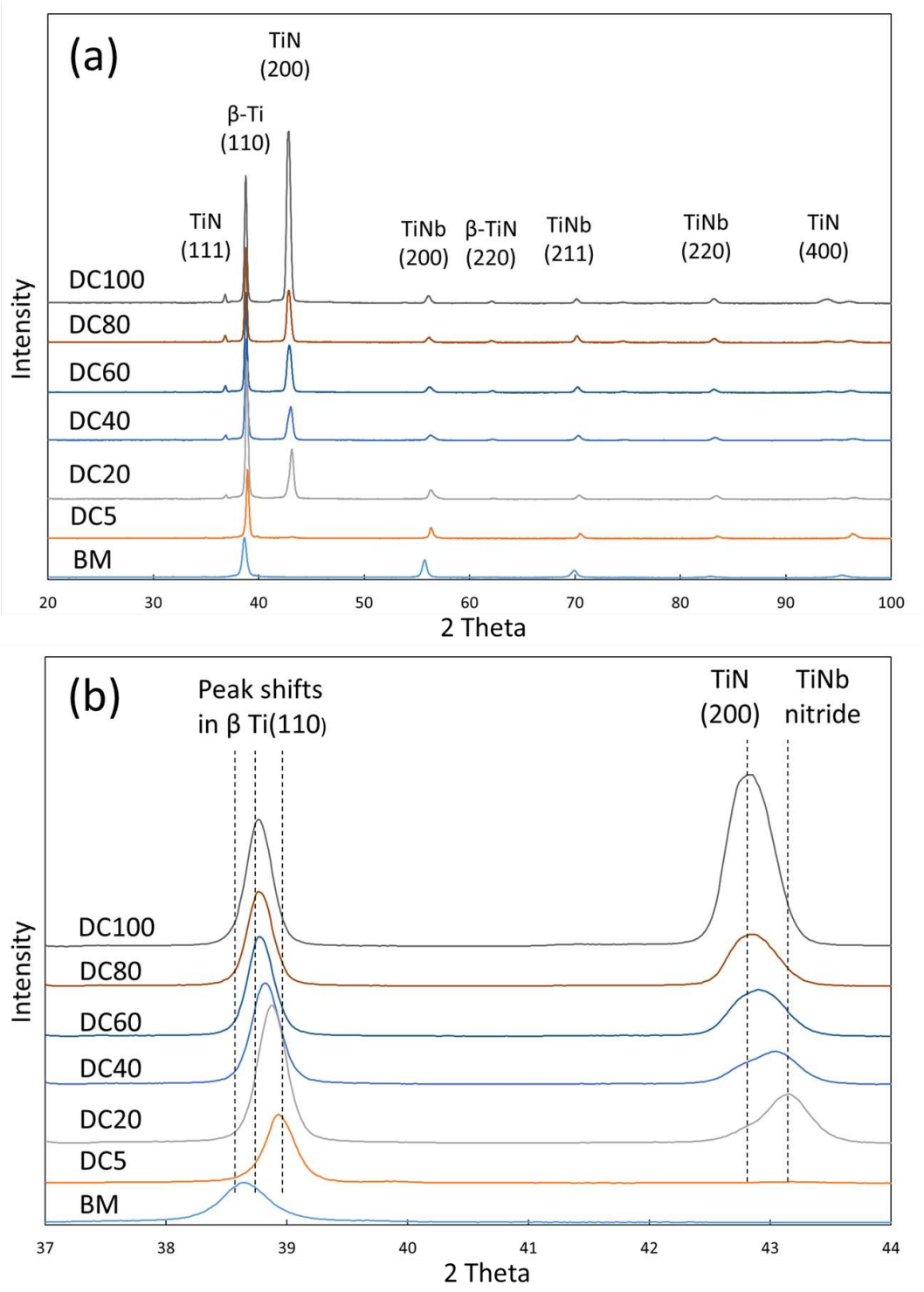

Figure 1. XRD spectra for the BM and laser-nitrided samples (a) from the diffraction angle between 20° and 100° (b) the enlarged view for the diffraction angle between 37° and 44°.

It is important to note that a more comprehensive and deeper investigation on the phase structure

of the samples nitrided between DC40 and DC100 had been reported in our recent study (Chan et. al. 2020). The focus of the phase structure study in this work was to characterize and understand the transition of phases when the TiNb samples were subjected to lower levels of duty cycles, namely DC5 and DC20.

As shown in Figure 2, the BM had a prominent peak at 38.7° (β 110) and additional weaker peaks present at 55.9° (β 200) and 70.1° (β 211). All laser-nitrided samples possessed these peaks but with reduced intensity. All of these peaks were associated with beta phase of Ti as a result of the presence of beta phase establishing element, i.e. Nb in the substrate. In addition to the main peaks which can be found in BM, it is noted that new peaks appeared at approximately 36° (TiN 111), 43° (TiN 200) and 62.5° (TiN 220) on the surfaces after laser nitriding. The intensity of these peaks became stronger with increasing duty cycle. The strongest intensity of peak at ~43° (TiN 200) belonged to DC100. However, these peaks were absent from the sample nitrided at the lowest duty cycle of DC5. Thus, we can conclude that no nitrides were formed in the surface of DC5. It is important to note that the TiN peak at ~43° shifted from 43.3° to 42.8° with increasing duty cycle from 20% to 100%. The peak at 43.3° indicates the presence of TiNb nitride (TiNbN). The surface nitrided at the duty cycle of DC20 contained mixed TiNb nitrides, whilst the surfaces of the higher duty cycle samples (DC40 to DC100) were more dominated by TiN. In addition, the peak of 38.7° (β 110) shifted to higher diffraction angle (~38.9°) when treating the sample at the duty cycle of 5% though no nitrided peaks were identified. This indicates that nitriding reactions took place on the surface of DC5 and led to the change of unit cell dimensions, but the laser energy and interaction time were not high and long enough to form nitrides at a level detectable by XRD.

Coverage of laser tracks after laser nitriding

With the setting of laser parameters addressed in the section 2.2, coverage of laser tracks showed a strong dependence on DC. For instance, Figure 3 shows the micrographs of the laser-nitrided samples at DC5 and DC20 as processed by ImageJ software.

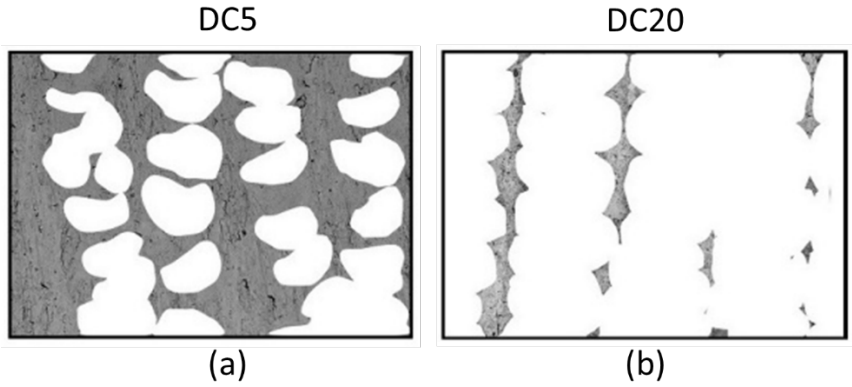

Figure 2. Micrographics of the laser-nitrided samples at lower duty cycles of 5% (a) DC5 and 20% (b) DC20.

In these images, the area that is higher than a threshold in z-direction (average basal plane) is expressed as white color, whereas the gray area reveals the morphological features of BM. Thus, the white areas represent the areas covered by laser tracks. As can be observed in Figure 3, the samples treated at DC5 and DC20 had a large portion of BM areas not covered by the laser-tracks. The same image processing for DC40 to DC100 showed all white and indistinguishable images (not shown), suggesting a full coverage of laser tracks for these samples. In fact, analysis of images for DC40 to DC100 by another mode of ImageJ showed increasing overlapping areas between the laser tracks with increasing duty cycle from 5.4%(DC40) to 24.8% (DC100) (Chan et al., 2020).

Surface roughness and topography before and after laser nitriding

Figure 4 provides the results of arithmetical mean height (Sa) and maximum height (Sz) of the samples nitrided at different duty cycles between 5% and 100%. Sa and Sz are the extension of Ra (arithmetical mean height of a line) and Rz (maximum profile height of a line) to a surface.

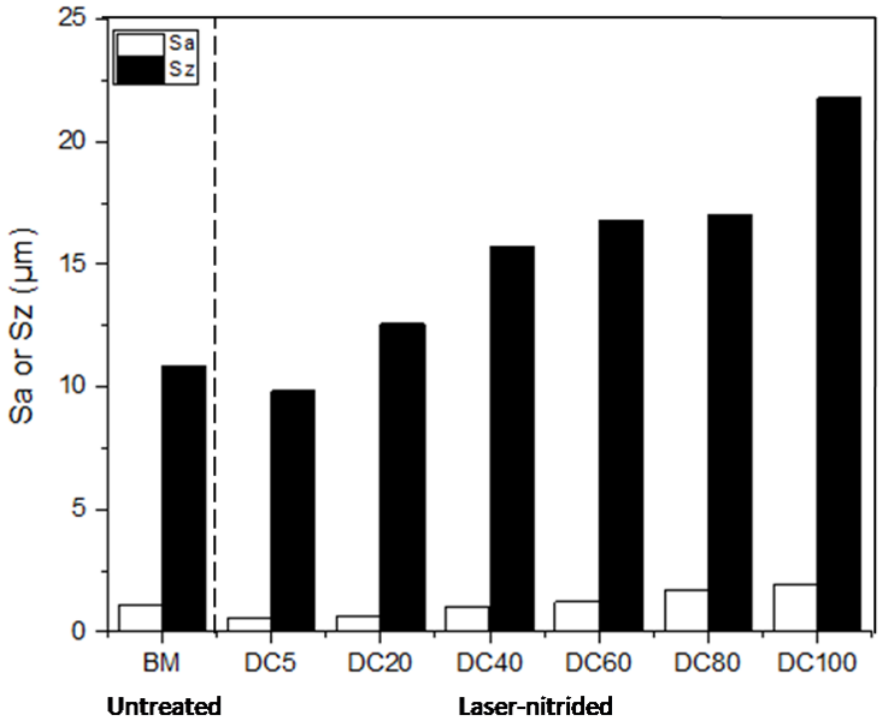

Figure 3. Comparison of Sa and Sz values between the BM and laser-nitrided samples of DC5 to DC100.

The BM sample (i.e. polished with 1000 grit SiC paper) was used as a control and had Sa of 1.059 μm and Sz of 10.833 μm. The Sa for the laser-nitrided samples lied between 0.536 μm and 1.904 μm whilst their Sz ranged between 9.814 μm and 21.767 μm. The results in Figure 4 indicate that both the Sa and Sz values of the nitride sample at the lowest duty cycle (DC5) were smaller compared with BM. The lower Sa compared to BM was observed also from the nitrided samples of DC20 and DC40. But, slightly different trend was observed in Sz in that all the samples nitrided at the duty cycles of 20% and higher showed higher Sz values than BM. For the laser-nitrided samples, the Sa values steadily increased with increasing duty cycles. As increasing trend occurred for the Sz values with increasing duty cycles, but the increase of Sz from DC60 to DC80 was very small whilst DC100 exhibited a sharp increase of Sz.

Compared with BM, the smaller Sa and Sz in DC5 can be explained by the effect of "laser polishing", i.e. the surface irradiated by short laser pulses at a power density which causes shallow

surface melting (only happened on the surface region of the substrate), thus resulting in the surface with fine-scale roughness (Giorleo, et al., 2015). With longer laser pulses and higher power densities at higher duty cycles (DC20 and higher), deeper surface melting occurs and this can result in stronger convection currents in the melt pools and thus rougher surfaces. The different trends in Sa and Sz can be explained by the difference in the calculation details of the two roughness parameters. Sa describes the arithmetic average height of the surface features within the defined area whilst Sz provides the average of the height difference between the five highest peaks and five lowest valleys within the defined area. In other words, surface roughening by laser at low DC scheme, e.g. DC20 and DC40, tends to generate distinct high peaks and valleys first before rather even surface roughness is generated. Figure 5 shows the 2D and 3D surface topography as well as the 2D roughness profiles of the samples before and after laser nitriding at different duty cycles between 20% and 100%.

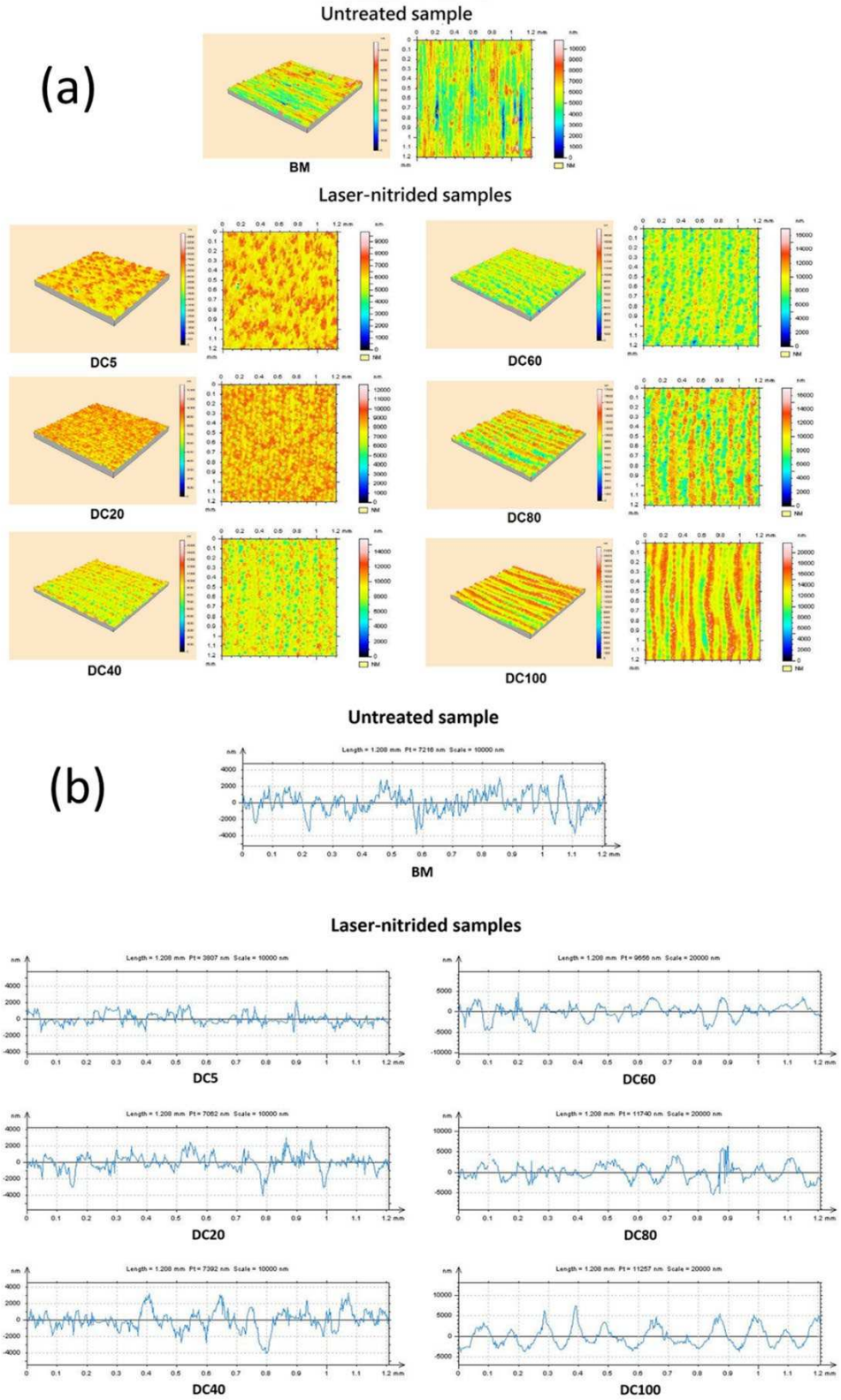

Figure 4. (a) The 3D and 2D surface images and (b) the 2D roughness profiles of the untreated BM and different laser-nitrided samples measured by WLI.

It can be seen that the surface of BM had distinct line patterns as a consequence of marks left by polishing during the metallurgical preparation process. In comparison, randomly distributed peaks and troughs (represented by the red and yellow patterns in Fig. 5) appeared on the surface of DC5, which can be correlated with the effect of laser nitriding at the lowest duty cycle. With increasing duty cycle, another line pattern started to appear on the surface of DC20, and apparently, this is due the laser tracks, not that from polishing marks. Because of the exposure of untreated area in DC20, the line patterns of laser tracks in DC20 were less obvious when compared with the samples nitrided at higher duty cycles (40% or above). The 2D roughness profiles in Figure 5 reveal more distinctive contrasts between the peaks and valleys of the line patterns in the surfaces nitrided between DC40 and DC100. With the increasing duty cycles, the line patterns appear to be more periodic with a reduction of "noise" (or roughness due to the existence of surface features in a finer scale) in the profiles.

Based on the combined studies of XRD and surface morphology, we suggest that during the process of laser nitriding of TiNb, the heat input of laser energy firstly caused the re-melting of substrate metals (Ti and Nb), followed by thermochemical reactions between N_2 and Ti in the substrate metals, leading to the formation of TiN on the surface. When the surfaces were nitrided at the lower duty cycles, namely DC5 and DC20, the shorter interaction time between the laser energy and substrate metals, along with the lower energy input, induced smaller melt pools. The laser spots (DC5) and tracks (DC20) formed after re-solidification were not large and wide enough to overlap with each other, and thus untreated BM area were still exposed on the surfaces. With increasing laser energy input and interaction time with increasing duty cycles (DC40 and above), the size of melt pools increased and the width of laser tracks also increased, leading to a more significant overlapping between the laser tracks. The duty cycle of 80% was found to be the threshold at or above which can cause a significant increase of overlapping between the laser tracks. When the laser tracks significantly overlapped, they tended to "crush" with each other and thus produce "peaks" where the roughest regions can be recognized on the surfaces of DC80 and

DC100. A detailed explanation to the structure of the fully-covered samples, namely DC40 to DC100 had been reported elsewhere (Chan et al., 2020).The findings indicated that minimum overlapping between the laser tracks would give desirable results to obtain the crack-free surface.

3.2. Functional Properties

As a result of nitriding TiNb samples with the laser treatment, several functional properties are expected to be changed. Among them, critically important as bearing materials of prosthetic joint implants studied in this study are hardness, tribological properties, and anti-microbacterial properties.

Vickers micro-hardness in cross-sectioned surfaces

Based on the results from the coverage of laser tracks, surface roughness, and topography measurements presented above, the samples nitrided at different duty cycle conditions can be categorized into the following groups: surfaces not fully covered by the nitride tracks (DC5 and DC20), fully covered surfaces with lower surface roughness (DC40 and DC60) and with higher surface roughness (DC80 and DC100). Figure 6 shows the OM images of the cross-sections of nitrided samples with the indentation marks for micro-hardness measurements.

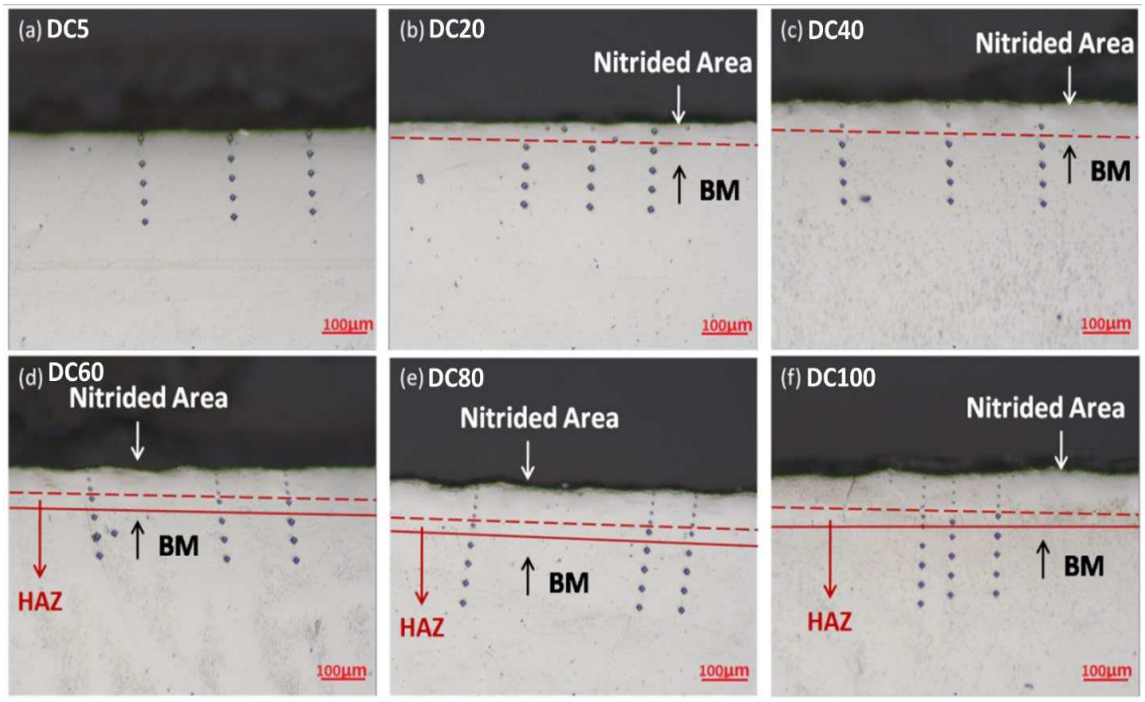

Figure 5. OM images of the cross-sections of nitrided samples with the indentation marks for micro-hardness measurements.

Briefly, remelted pool with semicircular shape started to become apparent from DC40, and the depth of re-melted pool increased with increasing DC; the thickness of the re-melted pool was determined from 22 μm (DC40) to 43 μm (DC100) (Chan et al, 2020). A trace of this microstructural feature is also visible from DC20, yet it is missing in DC5. Further detailed microstructural features of the nitrided samples were characterized by acquiring scanning electron microscope (SEM) micrograph images and are presented in Supplementary Material (S3, Figure S1). In addition, in-depth discussion on the microstructures of fully covered samples, DC40 to DC100, are available in a previous study (Chan et al, 2020). The results of hardness measurements along the cross-sections of laser-nitrided samples are presented in Figure 7.

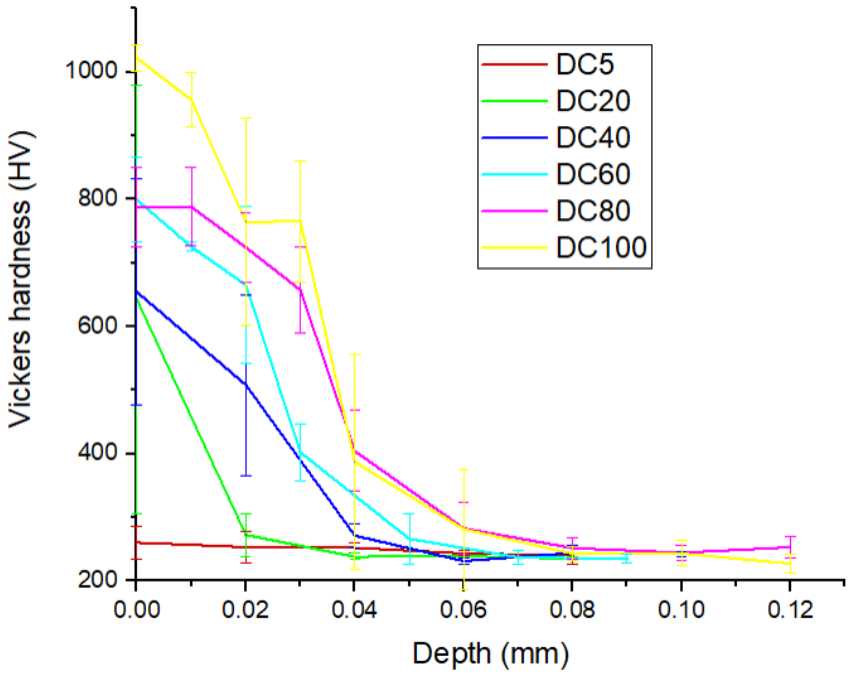

Figure 7. Results of Vickers hardness measurement along the cross sections of the laser-nitrided samples. The number of repetitions of the indentations at each depth was five (n = 5).

The first indentation mark was made at the points as close as possible to the top surface layer, from which the maximum hardness was obtained for all samples. The DC5 and DC20 (not fully covered group) had the maximum hardness ranged between 260 and 642 HV. The sample group of fully covered surfaces with relatively lower surface roughness (DC40 and DC60) had the maximum hardness between 654 and 799 HV, whereas those with relatively higher surface roughness had the maximum hardness between 788 and 1022 HV. Overall, the maximum hardness (recorded in the first indent mark) increased linearly with increasing duty cycle. Except for DC5, the hardness tended to decrease along with the measurement points, and the extent of decrease in hardness varied according to duty cycle conditions. For instance, the hardness of DC20 dropped sharply from 642 to 272 HV when the measurement point moved from the top surface region to the region at 0.02 mm in depth. Beyond that, the hardness values became steady at ~238 HV. The hardness profiles of DC40 and DC60 showed a smoother decreasing transition in hardness from

the top surface region down to the region of 0.05 mm in depth. For both samples, the hardness values no longer changed and stabilized at ~237 HV from 0.06 mm in depth. In contrast, the hardness of DC80 and DC100 started to drop rapidly from the maximum values (at the top surface region) until it reached to the steady value of 243 HV at the depth of 0.08 mm. Lastly, all the data points at and beyond the depth of 0.08 nm, ranging ca. 237 to 243 HV represent the hardness of BM.

The decreasing trend of hardness along the cross-sections is common to different nitrided samples and is attributed to the microstructural changes in TiNb after laser nitriding, namely from the remelted zone to HAZ, and then from the HAZ to BM, from the top surface to bulk. Detailed microstructural changes, in particular as a result of the change in duty cycles in laser-nitriding, had been reported in the authors' recent study (Chan et al., 2020). Briefly, the hardening effect in TiNb after laser nitriding can be associated with the following factors: (i) extent of overlapping between the laser tracks, (ii) thickness of the re-melted zone, (iii) concentration of TiN dendrites formed in the remelted zone, and (iv) presence of N-rich Ti in the remelted zone and HAZ. The role of increasing duty cycle is to induce an increase in both the thickness of remelted zone and the concentration of TiN dendrites, leading to higher hardness at the top surface region. It is important to note that hardness was fairly low and constant in DC5 sample throughout the cross section. This can be explained by the fact that no TiN was present in the remelted zone as evidenced by the XRD results in Figure 2. Furthermore, the depth of remelted zone was very shallow that its influence on the hardness is little to none. Moreover, since the laser tracks were not fully overlapped, some indentation marks in DC5 out of repetitive measurements could have been acquired from the untreated BM region, instead of the remelted zone. This could have also happened in DC20 with a lower probability.

Coefficient of friction (COF) of the nitrided surfaces

Pin-on-disc tribometry tests (a total sliding distance of 1,000 m under 10 N load) were carried out to investigate the frictional properties of the laser-nitrided sample surfaces. The untreated BM

samples were tested too as a control. All measurements were conducted in FBS as a model synovial fluid. The COF plots vs accumulated sliding distance for the BM and laser-nitrided samples are shown in Figure 8.

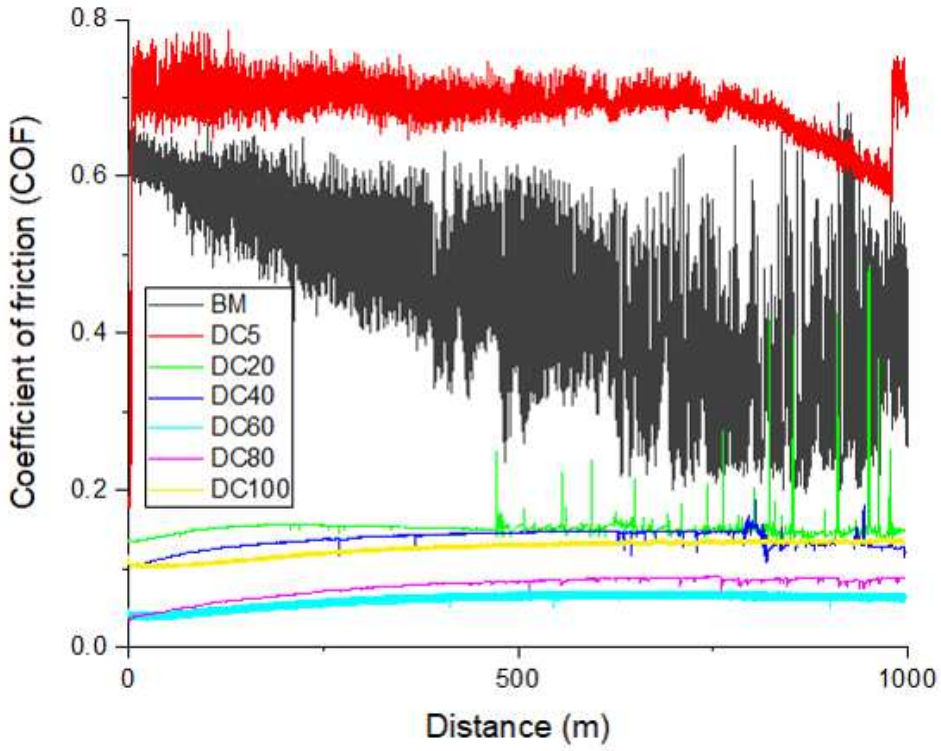

Figure 8. The COF vs sliding distance for the BM and laser-nitrided samples throughout the sliding tests.

It is evident that BM and DC5 showed much higher values and larger variations in COF compared to the other nitrided samples throughout the entire measurement. This result is similar to recent studies of laser-nitriding of other types of Ti or Ti-alloys (Filip, 2008), and indicates that the friction-lowering effect of nitride layers on Ti or Ti-alloy substrate is generally observed regardless of the purity or types of alloying elements. This can be firstly correlated with the significantly increased hardness due to the formation TiN layer on the surface as shown in Figure 6 and 7. Additionally, increased hydrophilicity TiN compared to BM, and thus a better wetting by water-based fluid, was suggested as another contributing factor too (Serro et al., 2009). For all the

other samples, the friction signals were fairly stable and lower than ca. 0.18 throughout the measurements, except for frequent spikes observed form DC20 from ca. 500 m sliding distance. Nevertheless, these samples, i.e. DC20 to DC100, still showed relative differences from each other in COF values. In order to compare and see whether there is any relation between the frictional properties and hardness or duty cycle, the mean COFs over the entire 1,000 m sliding distance are compared in Figure 9.

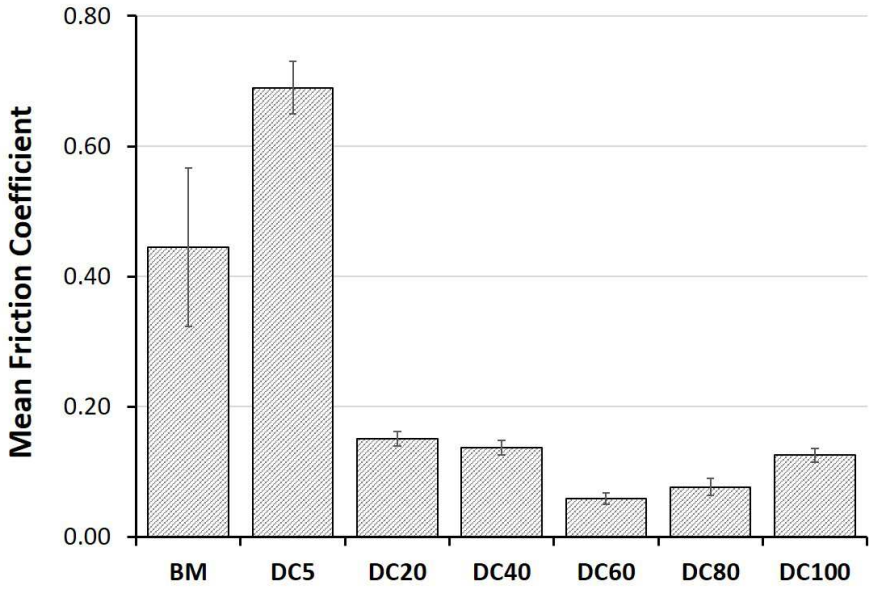

Figure 9. The mean coefficients of friction (COF) of the untreated BM and laser-nitrided samples.

Among all the samples, DC60 showed the lowest COF which represents a reduction by 87% compared with the BM. Meanwhile, both groups of samples with lower DC (DC20 and DC40) or higher DC (DC80 and DC100) than DC60 showed slightly higher COF values. Given that the hardness is gradually increasing with increasing DC (Figure 7), whereas the surface roughness is also increasing with increasing DC (Figure 4), we can firstly propose that the optimum frictional properties observed from DC 60, i.e. the lowest COF, are a compromise of the two opposing trends. Lastly, it is interesting to note that between the two samples showing the highest COFs, namely BM and DC5, the COF of DC5 is notably higher than that of BM, despite that the former was

lightly laser-treated. The delicate differences in the frictional properties of the nitrided samples under varying duty cycle will be further discussed below.

Wear resistance of the nitrided surfaces

Figure 10 shows the photographic pictures of the BM and laser-nitrided samples after the pin-on-disc tribometry tests.

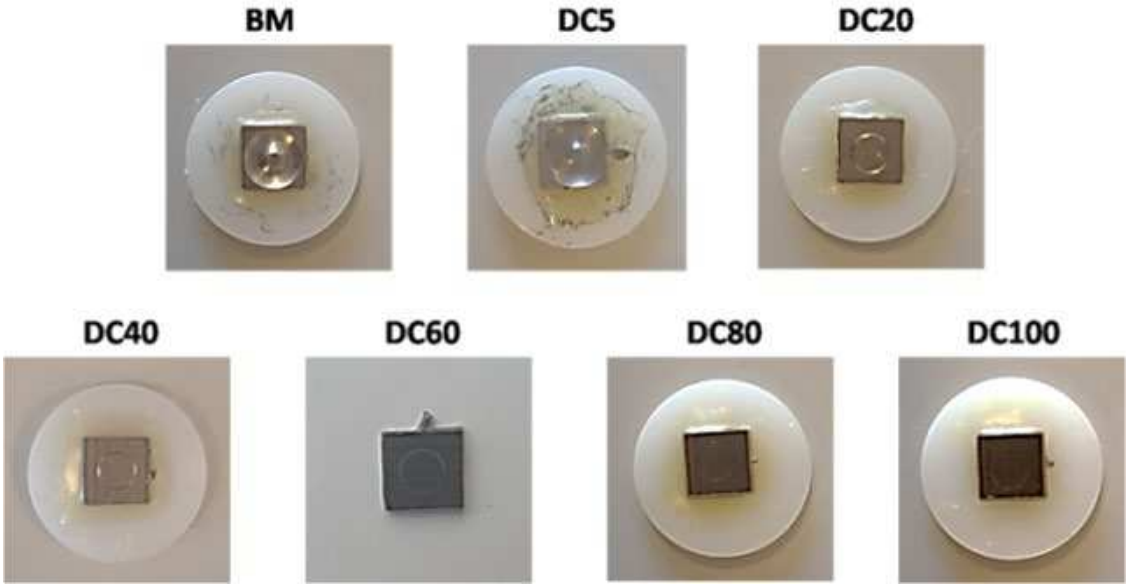

Figure 10. Photographic pictures of the untreated and laser-nitrided samples after the sliding tests.

Notable differences can be seen from BM and DC5, both of which displayed the surfaces undergoing a very severe wear as noted by the wide and deep sliding tracks. In addition, "squeaking" noise was heard during the sliding tests for BM and DC5, indicating the intense tribological contacts between the sapphire ball and the sample surfaces. Figure 11 shows a magnified OM image of the wear mark of BM after the pin-on-disk tribometry test.

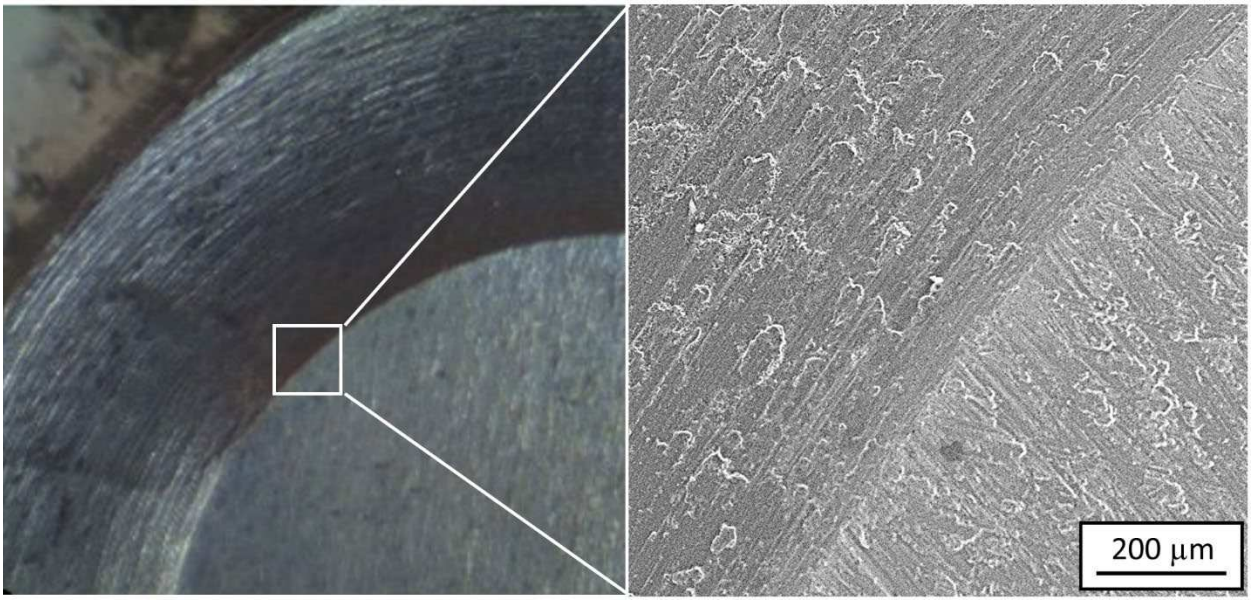

Figure 11. A magnified OM image of the wear track in BM after the pin-on-disk tribometry test. The SEM image on the right shows the magnified micrograph of the boundary between the wear track and prinstine BM.

The right SEM micrograph in Figure 11 displays the inner details of the wear mark. The wear track in BM was very deep with a clear directional sliding pattern. In contrast, the wear track is remarkably shallower and narrower for DC20 sample. With further increase of duty cycles to 40% and higher, the surfaces showed even shallower and narrower wear tracks. Figure 12a shows the magnified OM images of the wear tracks on the fully covered surfaces (DC40 to DC100) after the pin-on-disc tribometry tests.

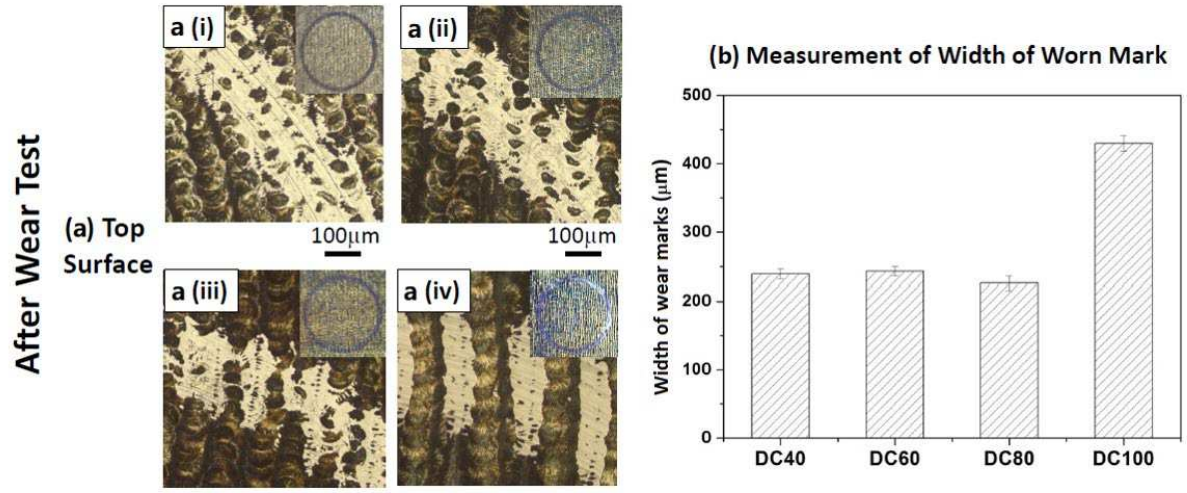

Figure 12. (a) The magnified OM images of the wear marks observed from the laser-nitrided samples, which are fully covered by laser tracks (a(i) DC40, a(ii) DC60, a(iii) DC80, and a(iv) DC100)after the pin-on-disk tribometry tests. The insets show the overview of the wear marks (b) The widths of the wear marks measured in Figure 8 by ImageJ (n = 18) are shown in (a).

The measured widths of the wear tracks on the DC40 to DC100 surfaces are shown in Figure 12b. There is no obvious difference in the wear track width for the samples ofDC40 toDC80, and the values were around 250 μm. In contrast, DC100 showed a clearly higher wear track width of 450 μm when compared with other fully covered samples. Furthermore, the wear marks on DC100 surface were found to be disconnected with each other. A similar, yet less serious phenomenon was found from the wear marks on DC80 surface. The wear marks in DC40 and DC60 were connected to form a continuous circular track. This qualitative difference in the patterns in wear marks according to duty cycle can also be correlated with increasing surface roughness with increasing duty cycles (Figure 4). The samples with higher surface roughness tend to expose higher gap between peaks and valleys, and thus it is more likely to display disconnected wear patterns after tribological stress on the surface.

The OM cross sections of the wear tracks in DC20 and DC100 are given in Figure 12.

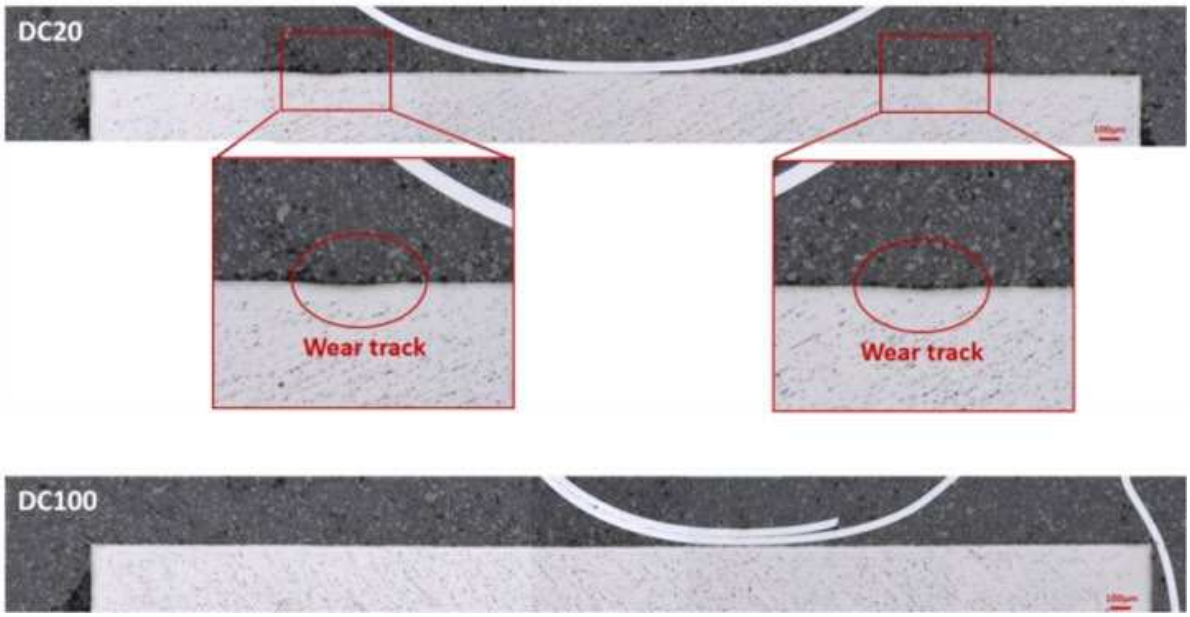

Figure 6. OM images of the cross-sectioned surfaces of DC20 and DC100 after the pin-on-disc tribometry tests highlighting the locations of wear tracks in the cross-sections.

As seen in Figure 13, a weak wear mark can be identified in the cross section of DC20. In contrast, similar feature is absent from the cross section of DC100, implying the worn mark was very shallow that cannot be identified by an optical microscope. In general, wear volume is related with hardness according to the following equation:

$$V = kLS/H \qquad \text{(eq. 1)}$$

where V is wear volume, k is wear coefficient, L is constant load, S is sliding distance and H is hardness. The wear coefficient k is usually considered to be constant in specific condition (Rigney, 1994). According to this equation, wear volume is expected to be inversely proportional to the surface hardness. The hardness measurement results in this study predict that the nitrided samples with higher duty cycle may display lower wear volume. Unfortunately, though, as the wear marks were not apparent for many nitrided samples as shown in Figure 13, it was not possible to determine the wear volume by profilometry and verify the relationship in eq. 1.

Debris size distribution after the sliding tests

An alternative to characterize the wear volume of the substrate is to characterize the wear debris released to the fluid, i.e. FBS, in which tribological contacts took place. Figure 14 shows the photographic pictures of fetal bovine serum (FBS) solutions collected from the BM and laser-nitrided samples after the pin-on-disc tribometry tests.

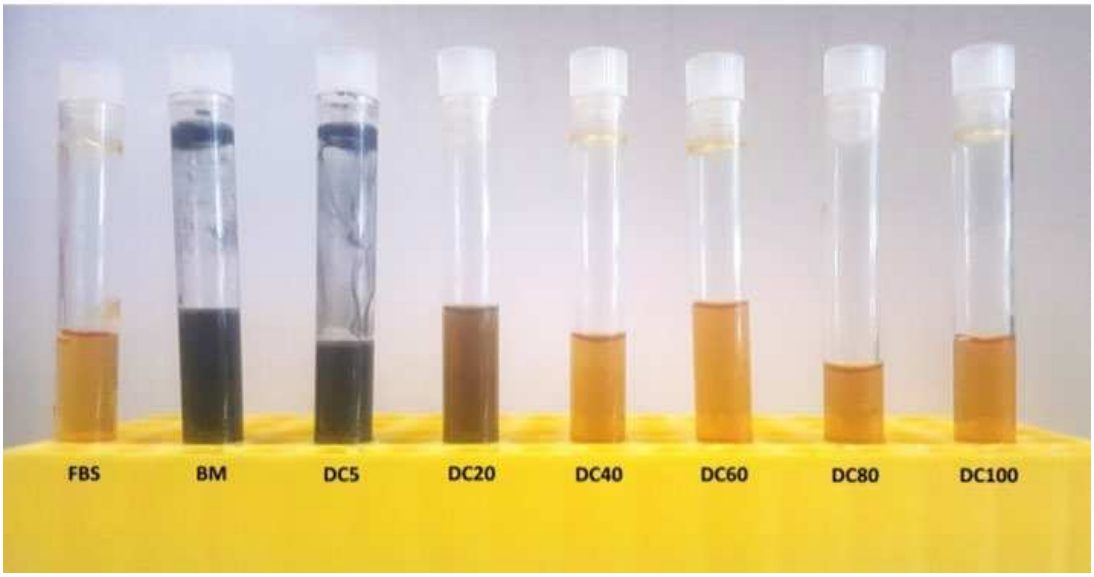

Figure 7. The FBS solutions collected from the BM and laser-nitrided samples after the pin-on-disc tribometry tests.

The FBS solutions displayed a recognizable colour changes across the samples due to the presence of wear debris with different chemical identity, size, and concentration in the solutions. The solutions of the BM and the sample treated with the lowest duty cycle (DC5) turned into black, indicating high concentration of wear debris. It is believed that the wear particles in DC5 were mainly composed of BM because a majority of the surface area exposed in DC5 was not laser-treated. The FBS of DC20 exhibited a dark brown colour, indicating either a lower concentration of wear debris and/or different chemical identity of wear debris compared those from BM and DC5. Given that surface coverage by nitrides is much higher for DC20 compared to DC5, the wear

debris is likely to be a mixture of the particles from the nitrided surface and the exposed BM on the surface. For the fully covered surfaces from DC40 to DC100, the solutions collected were clearer and nearly indistinguishable from the pristine FBS. Since the surfaces were fully covered by nitrides, the wear debris, if present, should be nitride particles and no BM particles were involved. Moreover, since nitride layer display a gold colour (Figure 12), it is expected to be more difficult to distinguish from the colour of pristine FBS even if they are present as wear particles in FBS.

Figure 15 provides the DLS profiles of particle size distribution of the FBS solutions collected from the BM and laser-nitrided samples after the pin-on-disc tribometry tests.

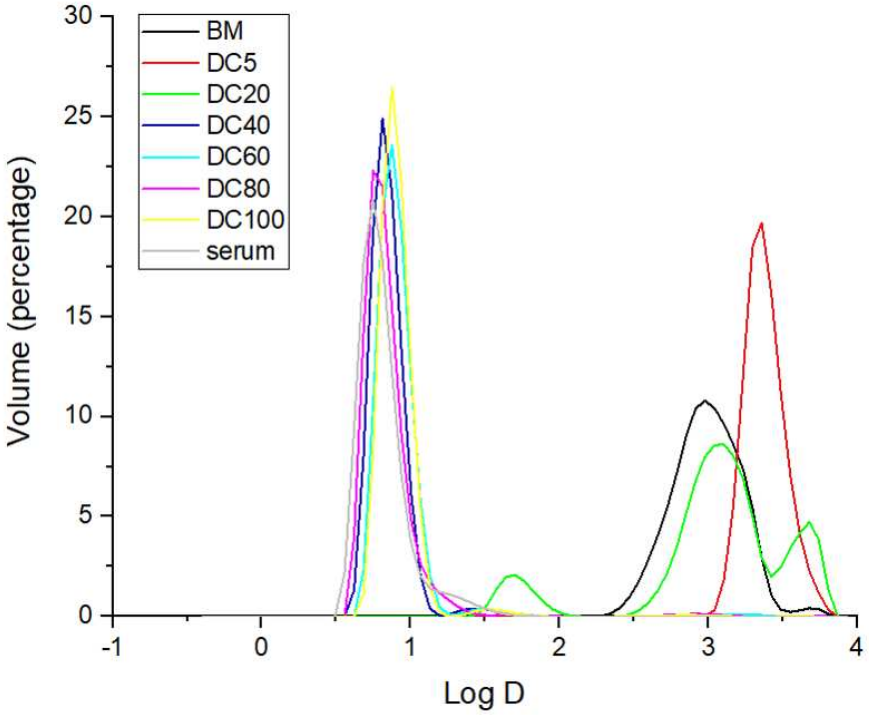

Figure 8. Size distribution of wear debris in the FBS collected from the BM and laser-nitrided samples after the pin-on-disc tribometry tests. The X axis (D) is the hydrodynamic diameter of wear debris whilst the Y axis is the volume of wear debris for each D.

The pristine FBS was used as a control as the proteins in FBS can also form detectable particles.

The fully covered samples from DC40 to DC100 showed similar profiles of size distribution compared to the pristine FBS in that only one distinct peak at around 10 nm was observed. It should be noted though that all of the peaks of the fully covered samples shifted to right compared with that of the pristine FBS, indicating the presence of nitride particles in the solutions. However, since the magnitude of shift is very small, the amount and size of wear particles from Ti alloy samples is expected to be small too. No particular trend is visible between the duty cycle and the particle size distribution for these samples. In contrast, the solutions of BM, DC5, and DC20 did not exhibit the peak at around 10 nm, but displayed much larger ones such as a broad single peak at around 1,000 nm for BM, a sharper single peak at around 2,000 nm for DC5, and multiple peaks at 50 nm, 1,000 nm, and 5,000 nm for DC20, all of which reflect more severe wear of these samples.

Another quantity to define the size of particles in solution by DLS is Z-average. The Z-average size values of wear debris in the FBS solutions collected from the BM and laser-nitrided samples are shown in Figure 16.

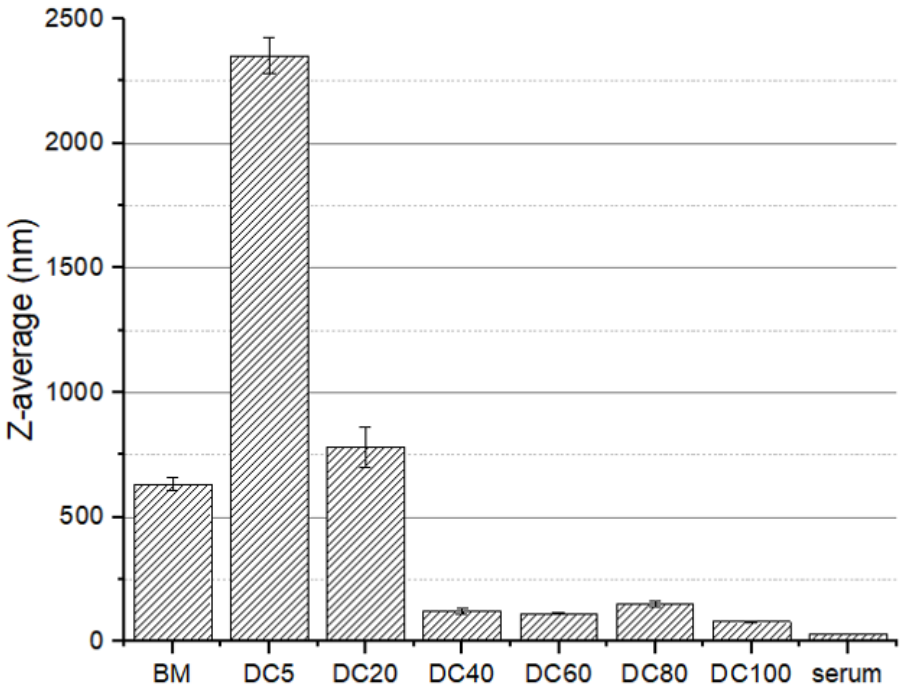

Figure 9. The Z-average size of the wear debris in the FBS solution collected from the BM and

laser-nitrided samples. The pristine FBS (or serum) was used as a control.

The Z-average size in DLS is a parameter known as the cumulative mean which is defined as the harmonic intensity averaged particle diameter. It is a hydrodynamic parameter and, strictly speaking, is applicable only to spherical and mono dispersed particles in solution. Basically, the same trend with the particle size distribution (Figure 15) was observed. A significant difference in the Z-average values was observed between the two groups of samples again, namely fully TiN-covered (DC40 to DC100) vs. BM or partially covered (DC5 and DC20) samples. The Z-average of the pristine FBS as a reference was 30 nm, and the highest Z-average value of 2,352 nm was observed from the solution of DC5. The Z-averages measured across the solutions from the DC40 to DC100 samples only slightly varied, and the values were very close to that of the pristine FBS.

One point that needs a further explanation is larger particle size distribution and higher Z-average value from DC5 than BM. In fact, this behavior is consistent with the higher COF observed from DC5 than BSM (Figure 8 and 9). This can be understood in the context of explaining the differences in wear mechanisms for BM, partially (DC5 and DC20), and fully-covered (DC40 to DC100) sample surfaces. To this end, a schematic illustration is provided in Figure 17.

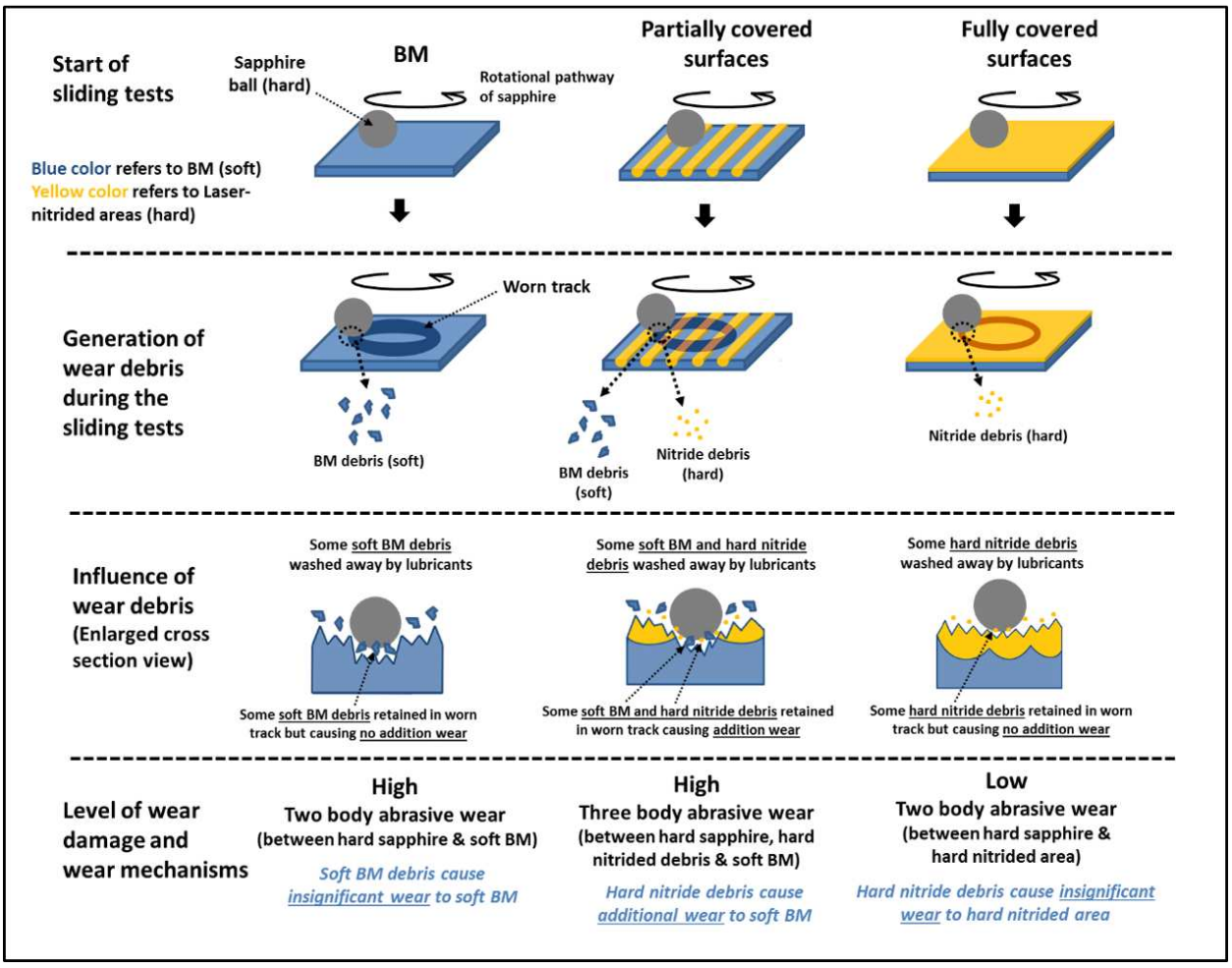

Figure 10. A schematic of the possible wear behaviours happened during the sliding tests for BM, partially and fully covered surfaces.

We propose that the wear processes occur in four stages: (i) start of the sliding contacts, (ii) generation of initial wear debris, (iii) influences of the initially generated wear debris on the wear track, and (iv) subsequent wear damage and the associated wear mechanisms. In the pin-on-disc tribometry tests, the sapphire ball, which was used as the slider, is harder (hardness 1600-1800 HV) (Goodfellow, 2019) than untreated TiNb (hardness 237-243 HV) or TiN (hardness 654-1022 HV) measured in this study. For BM, it is quite straightforward that the mechanism is two-body abrasive wear as the difference in hardness of sapphire ball and BM is very large. While initially generated Ti wear debris can be pressed against the flat BM surface, it is generally expected that this can lead to plastic deformation on the flat surface, and subsequent wear damage on the substrate, only when

the ratio between the hardness of particle (H_p) and substrate (H_s), i.e. H_p/H_s, is larger than 1.25 for spherical particles (Hutchings et al., 1992). Thus, Ti particles on Ti substrate or nitride particles on nitrided substrate are not expected to contribute further wear. A more complicated wear mechanism is expected for the partially covered surfaces as nitrides and BM co-existed on the surface, and accordingly, wear debris generated can be a mixture of harder nitride particles and softer BM particles. Thus, the hard nitride particles can press and cause additional wear damage on the soft BM substrate under sapphire ball. Therefore, the wear process for the partially covered surfaces is likely to be driven by a three-body abrasive wear. Most of all, local patches formed on DC5 surface from melting by laser treatment is expected to contribute to large-sized peak for the DLS profile for, if they are worn off from the surface (Figure 15). The two-body wear abrasive model is also expected to be dominant for the fully-covered surfaces as the contribution from the hard nitride particles to further wear of also hard nitride surfaces is ignorable.

Lastly, collective studies on hardness, friction, and wear properties of laser-nitriding of TiNb in this study showed that all three properties do not necessarily change in parallel as a function of duty cycle. For instance, the hardness of topmost layer of laser-treated TiNb was proportionally increasing with increasing duty cycle (Figure 7). In contrast, anti-wear properties of laser-nitriding as judged by size distribution of wear debris in FSB were nearly indistinguishable for the samples with duty cycle of 40% and higher (Figures 14-16), although the width of wear marks was notably higher for DC100 compared to DC40 to DC80 (Fig. 12b). Meanwhile, an optimum friction property (i.e. the lowest COF) were observed from DC60 (Figure 9). The lowest COF from DC60 can be firstly correlated with the interplay of hardness with increasing surface roughness with increasing duty cycle (Figure 4) as mentioned above. Another important factor to consider is micro-cracks generated from by the over-growth and populated TiN dendrites in the re-melted zones that were observed particularly more from the samples with very high duty cycle, e.g. DC80 and DC100 (Chan et al., 2020). In particular, the highest population of micro-cracks of DC100 may account for the notably larger width of wear marks compared to the other fully covered nitrided samples. It should be noted that even DC60 was not completely free from micro-cracks

on the surface. Since micro-cracks can be weak points to induce energy dissipation under shear stress, they can be additional factor for higher COFs from DC80 and DC100 compared to DC60. Moreover, when the applied tribostress is greater than that in this study, the samples with higher density of micro-cracks may display less effective wear-resistance too.

Bacterial adherence and biofilm formation on nitrided surfaces

The results of *S.aureus* adherence and biofilm formation on the BM and laser-nitrided surfaces after 24h culture are shown in Figure 18.

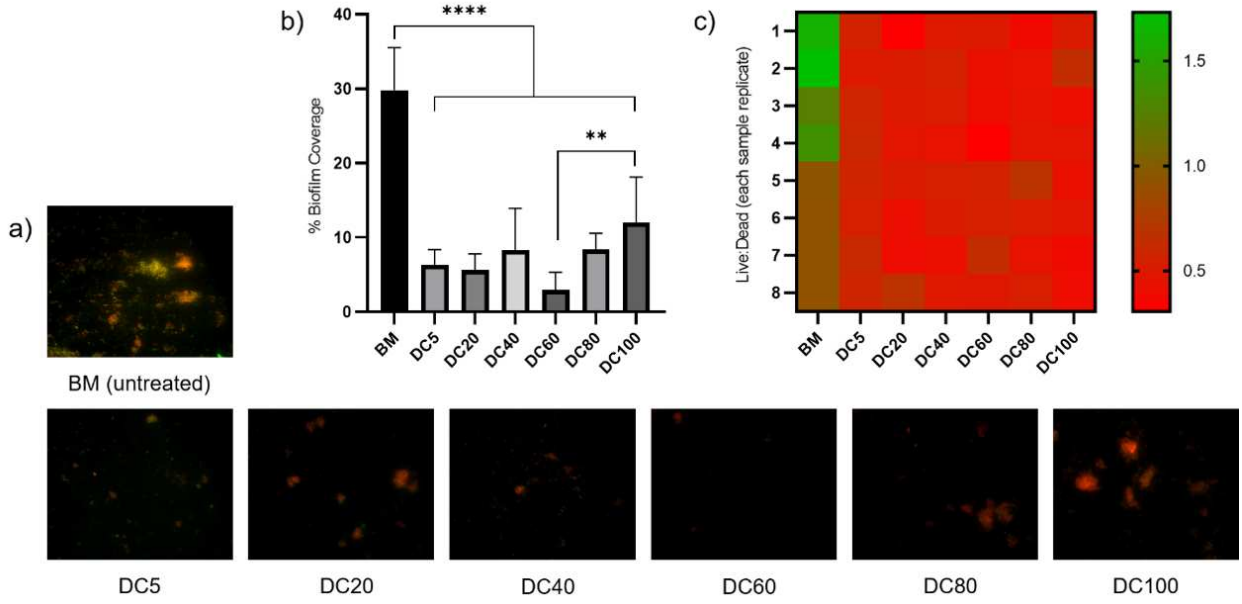

Figure 18. Bacterial coverage results for the BM and laser-nitrided surfaces after 24h culture with *S. aureus*. a) representative images showing bacterial adherence/biofilm coverage on each sample. Images were obtained by live/dead staining and fluorescence microscopy. Live (viable) bacteria are stained green, and dead (non-viable bacteria) stained red. b) Percentage biofilm coverage on each treated sample, and control material (BM) as determined by image analysis (* denotes significant difference). c) Ratio of live:dead bacteria on each image analyzed for each sample and BM control and data displayed as a heat-map. The scale shows samples with a greater proportion of live bacteria are represented in green, with greater proportions of dead bacteria represented in red.

The results in Figure 18 show a significant difference of total bacterial adherence/biofilm formation on the surfaces coverage the BM and the laser-nitrided samples ($p < 0.0001$). The BM sample had the highest biofilm coverage of 29.8%, and this total biofilm coverage was significantly decreased after laser nitriding. The laser-nitrided samples had the total biofilm coverage ranging from 2.9% (DC60) to 12.0% (DC100). Regarding the ratio between the dead and live bacterial cells, the portion of dead cells was always higher than the live cells on all of the laser treated samples. However, on the BM, a greater number of bacteria survive to colonize this surface, resulting in a greater proportion of live bacteria (green), and a hence greater percentage area of surface biofilm coverage. While all samples showed a significant reduction in adherent bacteria in comparison to control, the only intra-sample significance was shown between DC60 and DC100 ($p = 0.0012$).

The results in the XRD confirmed the existence of nitrides in the samples (DC20 to DC100) after laser nitriding, and the coverage of nitrides increased with increasing duty cycles. By increasing the duty cycles to 40% or above, the samples were fully covered by the nitride tracks. Moreover, the nitrides in the DC20 surface comprised mainly the TiNbN while those nitrided at 40% and above were covered mainly by TiN. Research by (Annunziata et al. 2011) and (Chan et al. 2017, Clare et al., 2020) reported that TiN coating is less attractive to the bacterial adhesion and proliferation, leading to an effective reduction in the biofilm formation. The initial bacterial adhesion and subsequent biofilm formation depend on the complex interplay between the (i) surface physical features (roughness and topography), (ii) chemistry of oxide layer (composition, structure or crystallinity and thickness) and (iii) wettability (Chan et al. 2018). The varying results in bacterial coverage across the samples nitrided at different duty cycle conditions are mainly attributable to the differences in the aforementioned factors. Regarding the DC5 sample, its surface after laser nitriding had no nitrides, but the surface properties were changed as a result of the localized surface melting caused by laser energy. An antibacterial oxide layer can be formed which reduced the bacterial coverage on the surface. The exposure of BM (uncovered regions) in the DC5, and also in the DC20 surfaces, could contribute to bacterial adherence on these samples. On

the other hand, DC80 and DC100 also had a higher bacterial coverage than DC60 despite that all three of them were fully covered with the nitride layers. Two reasons can be proposed; Firstly, it can be due to the presence of surface cracks in the nitride layers for higher DC samples, similarly with the higher frictional properties (DC80 and DC100) or the higher width of wear marks (DC100) discussed above. The cracks can potentially provide a niche for the bacteria to attach and colonize. Secondly, the higher roughness in terms of Sa and Sz for DC80 and DC100 can lead to greater opportunity for initial bacterial adhesion at the rough regions which possessed the features with higher height contrast, and thus result in a higher bacterial coverage on the surfaces.

Overall, DC60 displayed the best antibacterial properties compared with the other laser-nitrided samples. However, the micro-cracks on the surface of DC60 are still a concern when it is used for treating the bearing surfaces of an implant which mechanical motions are involved. Statistically, DC40 performed the same as in DC80 and DC100 but it is still inconclusive to explain why DC40 had an inferior antibacterial performance than DC60 provided that DC40 was fully covered by the nitride layer and no micro-cracks were present. A follow-up study is therefore required for further investigation.

4. Conclusions

A multifunctional, namely surface-hardened, anti-wear and anti-bacterial, layer was successfully created on the beta TiNb alloy by means of fibre laser nitriding in open air via the modulated mode. The important findings can be summarized as follows:

(i) The TiNb surfaces were laser-nitrided at different duty cycles between 5% (modulated module) and 100% (CW mode). The colour of the nitrided surfaces changed from silvery to gold colours in a different shade with increasing duty cycles. The nitrided surfaces were fully covered with nitride tracks upon laser nitriding at the duty cycle of 40% or above.

(ii) The surface nitrided at the lower duty cycle (DC20) contained mixed TiNb nitrides, whilst the surfaces of higher duty cycle samples (DC40 to DC100) were dominated by TiN. No nitrides were found on the surface of DC5.

(iii) The laser-nitrided surfaces had the Sa ranging between 0.536 μm and 1.904 μm, and the Sz lie between the 9.814 μm and 21.767 μm. The Sa and Sz values were found to be increasing with increasing duty cycles. The maximum hardness for the nitrided surfaces in the partially covered group (DC5 and DC20) was between 260 and 643 HV, whilst those in the fully covered group (DC40 to DC100) lie between 654 and 1022 HV.

(iv) The COF was found to be decreasing significantly upon nitriding the surfaces at the duty cycle of 20% or above. The surfaces nitrided at the duty cycle of 40% or above had the insignificant wear damage and generated the least amount of wear debris after the sliding tests.

(v) All nitrided surfaces exhibited an improved antibacterial performance against the bacterial attachment and biofilm formation of *S. aureus* after 24h culture, with the DC60 condition showing the lowest bacterial coverage.

Overall, it is instructive to find out that CW mode is not necessarily the best approach to form nitride layers in order to impart desired wear resistance and antimicrobial properties on beta-TiNb surfaces by means of fibre laser nitriding. As shown in this study, many samples with lower DC than 100%, such as DC60 is the sample modified with the optimum surface properties. It showed the lowest COF among all samples, lowest DLS size profiles together with some other samples, and the highest antibacterial properties. On the other hand, it should be also considered that DC40 may display even superior tribological functionalities under different load-bearing and shearing conditions than those in this study, as micro-cracks present in DC60, but not in DC40 (Chan et al., 2020), could be potentially the weak points to cause wear damage in long term.

References

Annunziata M, Oliva A, Basile MA, Giordano M, Mazzola N, Rizzo A, Lanza A, Guida L. (2011). The effects of titanium nitride-coating on the topographic and biological features of TPS implant surfaces. *Journal of Dentistry*, 39, 720-728.

Brien WW, Salvati EA, Betts F, Bullough P, Wright T, Rimnac C, Buly R, Garvin K. (1992). Metal levels in cemented total hip arthroplasty. A comparison of well-fixed and loose implants. *Clinical Orthopaedics and Related Research*, 276, 66-74.

Chan CW, Chang X, Bozorgzadeh MA, Smith GC, Lee S. (2020). A single parameter approach to enhance the surface quality of beta Nb-rich Ti-Nb alloy for orthopaedics via open-air fibre laser nitriding. *Surface and Coatings Technology*, 383, 125269.

Donaghy CL, McFadden R, Kelaini S, Carson L, Margariti A, Chan CW. (2020). Creating an antibacterial surface on beta TNZT alloys for hip implant applications by laser nitriding. *Optics & Laser Technology*, 121, 105793.

Chan CW, Carson L, Smith GC, Morelli A, Lee S. (2017). Enhancing the antibacterial performance of orthopaedic implant materials by fibre laser surface engineering. *Applied Surface Science*, 404, 67-81.

Chan CW, Carson L, Smith GC. (2018). Fibre laser treatment of martensitic NiTi alloys for load-bearing implant applications: Effects of surface chemistry on inhibiting *Staphylococcus aureus* biofilm formation. *Surface and Coatings Technology*, 349, 488-502.

Filip R. (2008). Laser nitriding of the surface layer of Ti6Al4V titanium alloy. *Achieves of Materials Science and Engineering*, 30, 25-28.

Giorleo, L., Ceretti, E., Giardini, C. (2015). Ti Surface laser polishing: Effect of laser path and assist gas. *Procedia CIRP*, 33, 446-451.

Gundtoft PH, Varnum C, Pedersen AB, Overgaard S. (2016). The Danish hip arthroplasty registry. *Clinical Epidemiology*, 8, 509-514.

Goodfellow Inc, (2019). Material Information for Sapphire ($A_{l2}O_3$ 99.9). Retrieved from http://www.goodfellow.com/E/Sapphire.html. Accessed 8th Nov 2019.

Huang C, Zhang Y, Vilar R, Shen J. (2012). Dry sliding wear behavior of laser clad TiVCrAlSi high entropy alloy coatings on Ti–6Al–4V substrate. *Materials and Design*, 41, 338-343.

Hutchings IM, Shipway P. Tribology: Friction and wear of engineering materials, Ch. 6, Putterworth Heinemann.

Knahr K. Tribology in total hip arthroplasty, ISBN 978-642-19428-3.

Khan, MA, Williams RL, Williams DF. (1999). The Corrosion behaviour ofTi-6Al-4V, Ti-6Al-7Nb and Ti-13Nb-13Zr in protein solutions. *Biomaterials*, 20, 631-637.

Katayama S, Matsunawa A, Morimoto A, Ishimoto S, Arata, Y. (1985). Surface hardening of titanium by laser nitriding. *Laser Processing of Materials. Proceedings of a Symposium Held at the 113th Aime Annual Meeting*. 159-166

Labek G, Thaler M, Janda W, Agreiter M, Stöckl B. (2011). Revision rates after total joint replacement: Cumulative results from worldwide joint register datasets. *The Journal of bone and joint surgery. British volume*, 93, 293-297.

Man K, Jiang LH, Foster R, Yang X. (2017). Immunological responses to total hip arthroplasty. *Journal of Functional Biomaterials*, 8, 33.

International Centre for Diffraction Data. Newton Sq, PA, USA, PDF-2 Database.

Market Reports. (2019). Global Hip Replacement Devices Market Likely to Emerge over a period of 2019-2025. Available at: https://consumerreportsreview.com/global-hip-replacement-devices-market-likely-to-emerge-over-a-period-of-2019-2025. Assessed at 1st Oct 2019.

Niinomi, M. (1998). Mechanical properties of biomedical titanium alloys. *Materials Science and Engineering A*, 243, 231-236.

OECD Health Statistics, 2016; Eurostat Database.

Rigney, DA. (1994). The roles of hardness in the sliding behavior of materials. *Wear*, 175 63-69.

Samuel S, Nag S, Scharf TW, Banerjee R. (2008). Wear resistance of laser-deposited boride reinforced Ti-Nb–Zr–Ta alloy composites for orthopedic implants. *Materials Science and Engineering*, 28, 414-420.

Serro AP, Completo C, Colaço R, dos Santos F, Lobato da Silva C, Cabral JMS, Araújo H, Pires E, Saramago B. (2009). A comparative study of titanium nitrides, TiN, TiNbN and TiCN, as coatings for biomedical applications. *Surface and Coatings Technology*, 203, 3701-3707.

Song Z, Borgwardt L, Høiby N, Wu H, Sørensen TS, Borgwardt A. (2013). Prosthesis infections after orthopedic joint replacement: The possible role of bacterial biofilms. *Orthopedic Reviwes (Pavia)*, 5, e14.

Steven MK. (2004). The UHMWPE Handbook: Ultra-high molecular weight polyethylene in total joint replacement. Amsterdam, Elsevier.

Tamilselvi S, Raman V, Rajendran N. (2006). Corrosion behaviour of Ti6Al-7Nb and Ti-6Al-4V ELI alloys in the simulated body fluid solution by electrochemical impedance spectroscopy. *Electrochimica Acta*, 52, 839-846.

Wang ML, Sharkey PF, Tuan RS. (2004). Particle bioreactivity and wear-mediated osteolysis. *The Journal of Arthroplasty*, 19, 1028-1038.

Supplementary Material to the manuscript:

Optimization of anti-wear and anti-bacterial properties of beta TiNb alloy via controlling duty cycle in open-air laser nitriding

Xianwen Chang[a], Graham C. Smith[b], James Quinn[c], Louise Carson[c], Chi-Wai Chan[b*], Seunghwan Lee[*a]

aDepartment of Mechanical Engineering, Technical University of Denmark, DK-2800 Kgs. Lyngby, Denmark
bFaculty of Science and Engineering, University of Chester, Thornton Science Park, Chester CH2 4NU, UK
cSchool of Pharmacy, Queen's University Belfast, Belfast BT9 7BL, UK
dSchool of Mechanical and Aerospace Engineering, Queen's University Belfast BT9 5AH, UK

S1.

CALCULATIONS OF LASER FLUENCE FOR FIBRE LASER SURFACE TREATMENT:

The focal spot diameter ($d_{e^{-2}}$) can be obtained by *Equation (1)*:

$$d_{e^{-2}} = \frac{4\lambda f}{\pi D_{e^{-2}}} \times M^2 \qquad (1)$$

Where $d_{e^{-2}}$, λ, f, $D_{e^{-2}}$, and M^2 are the focal spot diameter, wavelength of the laser beam, focal length of lens, diameter of the beam before the lens, and beam mode parameter of the fibre laser

Given that λ, f, $D_{e^{-2}}$, and M^2 are 1.064 μm, 125 mm, 5 mm, and 1.2 respectively.
By substituting these values into *Equation (1)*, the focal spot diameter ($d_{e^{-2}}$) is 41 μm.
The laser spot diameter at the stand-off distance of 1.5 mm can be obtained using simple trigonometry. After calculations, it is 100 μm, and hence the spot area is 7.85 x 10^{-5} cm^2. The modulation frequency of the laser system is 100 kHz, and the laser power being used is 45 W.

Take a pulsed laser with a given output power. Pulsed lasers are modulated. Therefore, the energy of each pulse can be calculated by *Equation (2):*

$$Pulse\ \ Energy\ \ (J) = \frac{Laser\ \ Power\ \ (W)}{Modulation\ \ Frequency\ \ (Hz)} \qquad (2)$$

The laser fluence (J/cm^2) can be calculated by *Equation (3)*:

$$Laser\ \ Fluence\ \ (J/cm^2) = \frac{Pulse\ \ Energy\ \ (J)}{Spot\ \ Area\ \ (cm^2)} \qquad (3)$$

By substituting the values into *Equation (2) and (3)*, the laser fluence at the power of 45 W with the modulation frequency of 100 kHz is 5.7 $\mathrm{J/cm^2}$

S2.

The apparent contact pressure can be estimated from the mechanical properties and contact geometry based on the Hertizian contact pressure equation.

Sapphire
Elasticity modulus 345 GPa, Poisson ratio 0.25, r = 3 mm
REF) http://valleydesign.com/sappprop.htm

TiN
Elasticity modulus 260 GPa, Poisson ratio 0.25
REF) https://www.memsnet.org/material/titaniumnitridetinfilm/

TiNb
Elasticity modulus 90 GPa, Poisson ratio 0.25
REF) On the mechanical properties of TiNb based alloys, Journal of Alloys and Compounds Volume 571, 15 September 2013, Pages 25-30. Please note that in this paper, the elasticity moduli of TiNb with Nb percentage of ca. 8% and 25% only (8 GPa) were provided. Since the percentage of Nb is higher for the sample in this study (45%), the value was adjusted in a linear way.
The apparent maximum Hertzian contact pressures are thus estimated to range from 2.78 GPa (sapphire ball/TiN pair) to 1.71 GPa (sapphire ball/TiNb (BM) pair) (Supplementary Material, S2)."

S3.

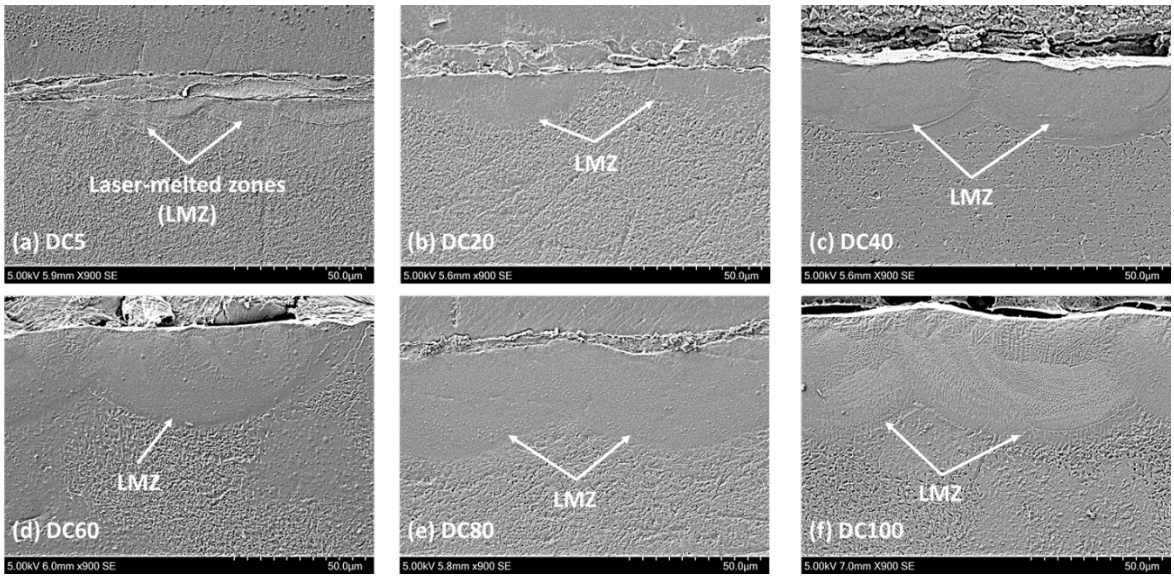

Figure S1. Scanning-electron microscope SEM (SEM, FlexSEM 1000, Hitachi, UK) micrographs for the nitrided samples. These images were captured in secondary electron (SE) mode at a lower magnification (x900) and 20-kV beam.